

Tuning of the ultrafast demagnetization by ultrashort spin polarized currents in multi-sublattice ferrimagnets.

Deeksha Gupta¹, Maryna Pankratova², Matthias Riepp¹, Manuel Pereiro², Biplab Sanyal², Soheil Ershadrad², Michel Hehn³, Niko Pontius⁴, Christian Schüßler-Langeheine⁴, Radu Abrudan⁴, Nicolas Bergard¹, Anders Bergman², Olle Eriksson^{2,5}, and Christine Boeglin^{1*}

¹Institut de Physique et de Chimie des Matériaux de Strasbourg, UMR7504, CNRS et Université de Strasbourg, 67034 Strasbourg, France

²Department of Physics and Astronomy, Uppsala University, Box 516, SE-75120 Uppsala, Sweden

³Institut Jean Lamour, Université Henri Poincaré, Nancy, France

⁴Helmholtz-Zentrum Berlin für Materialien und Energie GmbH, Albert-Einstein Str. 15, 12489 Berlin, Germany

⁵Wallenberg Initiative Materials Science for Sustainability (WISE), Uppsala University, Box 516, SE-75120 Uppsala, Sweden

* christine.boeglin@ipcms.unistra.fr

ABSTRACT

Femtosecond laser pulses can be used to induce ultrafast changes of the magnetization in magnetic materials. Several microscopic mechanisms have been proposed to explain the observations, including the transport of ultrashort spin-polarized hot-electrons (SPHE). Such ultrafast spin currents find growing interest because of the recent challenges in ultrafast spintronics, however they are only poorly characterized. One of the key challenges is to characterize the spin-polarized ultrafast currents and the microscopic mechanisms behind SPHE induced manipulation of the magnetization, especially in the case of technologically relevant ferrimagnetic alloys. Here, we have used a combined approach using time- and element-resolved X-ray magnetic circular dichroism and theoretical calculations based on atomistic spin-dynamics simulations to address the ultrafast transfer of the angular momentum from spin-polarized currents into ferrimagnetic $\text{Fe}_{74}\text{Gd}_{26}$ films and the concomitant reduction of sub-lattice magnetization. Our study shows that using a Co/Pt multilayer as a polarizer in a spin-valve structure, the SPHE drives the demagnetization of the two sub-lattices of the $\text{Fe}_{74}\text{Gd}_{26}$ film. This behaviour is explained based on two physical mechanisms, i.e., spin transfer torque and thermal fluctuations induced by the SPHE. We provide a quantitative description of the heat transfer of the ultrashort SPHE pulse to the $\text{Fe}_{74}\text{Gd}_{26}$ films, as well as the degree of spin-polarization of the SPHE current density responsible for the observed magnetization dynamics. Our work finally characterizes the spin-polarization of the SPHEs revealing unexpected opposite spin polarization to the Co magnetization, explaining our experimental results.

Introduction

Ferrimagnets are important materials in order to push spintronics and magnetic data storages towards the subpicosecond regime while ensuring low energy consumption. These materials are also among systems that show single pulse all optical switching, an important property for applications using ultrafast spintronics¹⁻⁵. Since more than 25 years, femtosecond laser pulses have been used as an ultrafast source of excitation to induce ultrafast changes in the magnetization, motivating many experimental and theoretical descriptions^{4,6-14}. In order to manipulate the magnetization in ferro- and ferrimagnetic films, ultrashort spin current pulses have

recently been revealed to be an extremely promising way for applications in ultrafast spintronics since they are known to launch ultrafast spin dynamics in different magnetic films with low heat dissipation¹⁵⁻²⁴. Such ultrafast spin currents can be launched using femtosecond laser pulses exciting ultrathin metallic films. This method of generating ultrashort currents has attracted increasing technological interest related to their ultrashort duration of a few hundred femtoseconds, which is compatible with subpicosecond manipulations of magnetization.

In previous works, ultrashort current pulses have been shown to flow between two ultrathin ferro- or ferrimagnetic layers^{19,25,26}, and they are able to produce subpicosecond demagnetization or picosecond switching without any external magnetic fields. Recently, specifically grown spin-valve structures with two separated magnetic layers have been used to produce spin-polarized hot-electron (SPHE) currents in a hard-magnetic layer. A second free (soft) magnetic layer is used to observe the induced dynamics. Several characteristic features can be extracted from the literature; for instance, the antiparallel orientation of both magnetic layers in the spin valve favors the hot-electron (HE) induced switching of the soft layer^{19,24}. Surprisingly, recent counterintuitive results revealed that other spin valve systems show switching in the soft layer only for a parallel orientation of the hard and soft layer¹⁹. Those results showed that the orientation for successful switching depends on fluence, which raises questions about the multiple mechanisms behind spin switching. These different results from the literature ask for a theoretical microscopic description of the mechanisms involved in the transfer of spin angular momentum between the SPHE current and the magnetic moments in ferro- and ferrimagnets. One of the first combined models one can think of to describe ultrafast demagnetization associates thermal induced reduction of the magnetic order with non-thermal angular momentum transfer. In multi-sublattice ferrimagnets, the role of spin current transfer is even more complex²⁷ since additional local mechanisms may emerge. For instance, local ultrafast transfer of angular momentum between two exchange coupled sublattices, suggested by Mentink et al.²⁸, has been confirmed by experimental observations²⁹. It evidences that during the ultrafast loss of magnetization in each of the sub-systems, the total angular momentum is conserved over a few hundred femtoseconds, involving two compensating angular momenta, which flow in opposite directions. The situation is drastically different and is expected to be more complex by using an excitation source of spin polarized currents with a pulse duration of a few hundred of femtoseconds, potentially transferring angular moment to the ferrimagnet during the first hundreds of femtoseconds.

The microscopic processes defining the ultrafast excitation by ultrashort spin currents of such complex multi-sublattice ferrimagnets thus need a detailed and microscopic understanding in the subpicosecond time scale. Among others, the information about the pulse energy density (or fluence), spin polarization, and pulse duration of the SPHE pulses is essential to describe the ultrafast excitations. It is indeed well documented that the pulse duration together with the pulse fluence are important parameters driving the ultrafast demagnetization and switching when excited by infrared (IR) or hot electrons (HE)^{30,31}. When using IR pump pulses, the duration of the pulse is well controlled and can be tuned to reach the desired thresholds (100 fs - 2 ps). The situation is more complex for ultrashort spin current pulses where the pulse durations are produced via diffusion and propagation through the films, leading to only indirect characterization of the pump duration and spin polarization. We estimate that the slightly longer pulses of HE of a few hundred of femtoseconds will not be detrimental to the angular momentum transfer in ferrimagnets because the demagnetization dynamics measured in those materials are much longer and last for almost 1 ps.

We report here on combined experimental and theoretical results evidencing the spin dependent hot electron (SPHE) induced demagnetization on the ultrafast time scale on Fe₇₄Gd₂₆ alloy in a specifically designed spin valve structure. We provide different quantitative numbers for pulse duration and spin polarization that characterize the hot-electron pulses. The experimental results were obtained by time-resolved X-ray magnetic circular dichroism (TR-XMCD) at the transition-metal (TM) L₃ and rare-earth (RE) M₅ edges at the BESSY II Femtoslicing source of the Helmholtz-Zentrum Berlin^{7,32,33}. This experimental method combines element and magnetic sensitivity³⁴⁻³⁶ with femtosecond time resolution, resolving the ultrafast magnetization dynamics in ferrimagnetic Fe₇₄Gd₂₆ alloys. Here, we give the first experimental results evidencing the timescales of the ultrafast quenching of the magnetization in ferrimagnetic Fe₇₄Gd₂₆, induced by ultrashort pulses of spin currents as produced in a collinear magnetic spin valve structure (CoPt / Cu / FeGd). In addition, it is reported here that, relying on experimentally defined geometry and composition as well as interatomic exchange, theoretical modeling based on atomistic spin-dynamics simulations reproduces the experimental ultrafast dynamics of this system. This fact allows to identify the microscopic process of spin angular momentum transfer at the shortest time scale^{14,37}. The proposed model is a combination of two processes: one is thermal in origin due to HE induced heating of the spin system, and the second is a non-thermal spin transfer torque

(STT) resulting from spin angular momentum transfer. Note that it is out of the scope of this paper to explicitly model the SPHE current generated from the Co/Pt multilayer. Currently, the physics governing the generation and transport is still under debate, and it is still speculated that multiple mechanisms are possible to generate such currents: hot electron spin filter effect through electron scattering, superdiffusive spin transport and magnon excitations via the ultrafast loss of angular momentum in the ultrathin Co/Pt multilayer^{12,13,15,17,38,39}.

As detailed below, the theoretical model employed here reproduces the experimental data and reveals how SPHE excitations drive the demagnetization in both sub-lattices of Fe₇₄Gd₂₆. Most noteworthy, the theoretical calculations reproduce the time scales and amplitudes of the experimental results recorded at Fe L₃ and Gd M₅ edges, leading to an indirect determination of the degree and of the sign of spin polarization in the SPHE current. This model can further be used to predict the impact of fluence dependent variations of the HE induced heating and of STT in both of the Fe₇₄Gd₂₆ sub-lattices.

Results

Experimental details

The sample structure used for the combined study of SPHE induced ultrafast demagnetization is shown in Fig. 1a. The sample is optimized so that the HE pulses are optically generated by ultrashort laser pulses using the Pt capping layer. The HE current pulses are then sent through the Cu(60nm) film, where the IR pulse is absorbed and through a hard-magnetic Co/Pt multilayer film, which generates ultrashort SPHE pulses^{17,22}. The SPHE induced ultrafast demagnetization can then be probed in a soft-magnetic Fe₇₄Gd₂₆ layer (detector) located at the bottom of the spin valve. The sketch in Fig. 1b shows the atomic Fe and Gd magnetic moments coupled antiparallel in Fe₇₄Gd₂₆. The alloy has a compensation temperature above 350 K, which is significantly higher than the sample temperature before the IR pump excitation ($t < t_0$). In Fig.1b, the blue arrow indicates the local Gd 4f moment, which can be aligned by an external magnetic field of moderate amplitude ($H=100$ Oe) well below the coercive field of the Co/Pt multilayer (600 Oe). The green arrow represents the local Fe 3d magnetic moment, exchange coupled so that it is antiparallel to the Gd-4f magnetic moment. Note that P (AP) defines the parallel (antiparallel) orientations between the magnetization of the Co/Pt multilayer and the Fe atomic magnetic moment in

$\text{Fe}_{74}\text{Gd}_{26}$ (Fig 1b).

The magnetic configuration at the thermodynamic equilibrium of the CoPt / Cu(10) / $\text{Fe}_{74}\text{Gd}_{26}$ spin-valve has been analyzed by X-ray magnetic circular dichroism (XMCD) measurements as a function of temperature, see Methods section. The 10 nm thick Cu film ensures no magnetic coupling between Co/Pt and $\text{Fe}_{74}\text{Gd}_{26}$ films. The spin valve is thus ideally suited to measure two relative spin-spin configurations by changing only the relative magnetizations in both magnetic films. Thanks to the chemical sensitivity of XMCD, our static measurements performed at the Gd M_5 and Co L_3 edges are used to define the sample temperature during the pump-probe experiments (for details, see Fig. 2 and 3 in Supplementary Information).

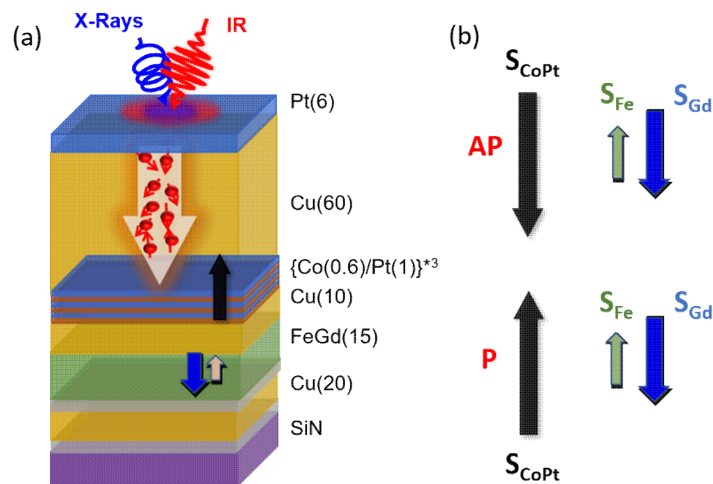


Figure 1. Spin valve structure and schematic representation of experimental scheme: (a)

Sample structure used to study the spin-polarized hot electron (SPHE) induced dynamics: SiN/Ta (5) /Cu (20)/Ta (5) / $\text{Fe}_{74}\text{Gd}_{26}$ (15) /Cu (10) / {Co (0.6)/Pt (1)*3}/Cu (60) /Pt (6). The thickness of each layer in the bracket is in nm. Here, the red pulse represents the IR laser (800 nm) of 60 fs duration acting as a pump, and the blue pulse represents the circularly polarized X-ray pulses of 100 fs duration as a probe. Both pulses are separated by 1° . The large arrow represents the direction of hot electrons flow, and inside, the short red arrow with a circle represents the non-polarized hot electrons. Cu (60) ensures the complete absorption of the IR pulse; therefore, the bottom Co/Pt layer is excited through HE pulses only. Consequently, those HE pulses generate spin-polarized current (SPHE) from Co/Pt. After crossing the spacer layer, the spin current

interacts with the $\text{Fe}_{74}\text{Gd}_{26}$ layer, on which the response of SPHEs is recorded. (b) Parallel (P) and antiparallel (AP) experimental scheme: The Black, green, and blue arrows represent the Co, Fe, and Gd spin moment orientation. AP and P define the relative orientations of the magnetization between Co and Fe spin moments in $\{\text{Co (0.6)}/\text{Pt (1)}\}^3$ and $\text{Fe}_{74}\text{Gd}_{26}$, respectively.

By measuring the hysteresis at Co L_3 and Fe L_3 edges (see inset of Fig.3a), we defined the saturation fields during pump-probe of both magnetic films (Co/Pt and $\text{Fe}_{74}\text{Gd}_{26}$) of 1000 Oe and 200 Oe, respectively. The X-ray transmission experiment, using an IR laser pump (red) and X-ray probe (blue) configuration, is schematically shown in Fig. 2. The external magnetic field is applied along the propagation direction of the X-rays (blue). The time $t_0 = 0$ is defined by the temporal overlap between the IR laser and X-ray pulses. The incident X-rays are circularly polarized. The TR-XMCD is extracted by making the difference of the transmitted X-ray absorption spectra intensities recorded by applying two opposite magnetic fields, +H and -H, parallel to the X-rays, as a function of time (see Methods). Alternating the pumped and the unpumped signals at the Fe L_3 and Gd M_5 edges allows for the normalization of the XMCD signal during the pump-probe delay scans. At the same time it allows to verify the magnetization at negative delay in the $\text{Fe}_{74}\text{Gd}_{26}$ film.

Ultrafast demagnetization in $\text{Fe}_{74}\text{Gd}_{26}$. The case of Fe.

In Fig.3, we show the pump-probe results obtained at the Fe L_3 edge of the $\text{Fe}_{74}\text{Gd}_{26}$ alloy layer at an IR fluence of $120 \text{ mJ}/\text{cm}^2$. The values at negative delays are normalized to 1. The continuous lines are the results of the fitting (see Methods). The inset of Fig 3a shows the (static) element selective hysteresis measured at the Co L_3 and Fe L_3 resonance edges during the pump probe experiment at negative delays. This data indicates that the coercivity of the Co/Pt layer ($H_c = 600$ Oe) is larger than that of FeGd ($H_c = 100$ Oe). The measurements in Fig.3a show the ultrafast demagnetization dynamic induced by the SPHE pulses where spins are parallel (P) to the magnetization of Fe (blue curve) and antiparallel (AP) (red curve) to the magnetization of Fe in the $\text{Fe}_{74}\text{Gd}_{26}$ alloy. Solid lines are the exponential fit with the Gaussian convolution. We have analyzed the demagnetization dynamics obtained at the Fe L_3 edge at two timescales: At short time scale (Fig.3a), i.e., below 2.5 ps, we find that the experimental dynamics in the parallel case (P) is faster and slightly larger in amplitude than for the AP case. Characteristic demagnetization times are extracted for P and AP cases and have values of 470 ± 80 fs and 550 ± 80 fs, respectively.

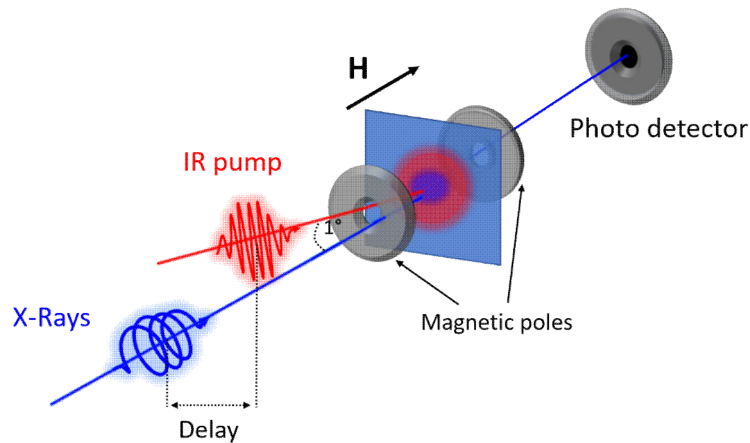


Figure 2. Schematic illustration of tr-XMCD pump-probe experimental set-up: Schematic of experimental set-up at Femtoslicing beamline, BESSY. IR laser (800 nm) of pulse width of 60 fs with a repetition rate of 3 kHz is used as a pump and ultrashort circular polarized X-rays of 100 fs duration and 6 kHz repetition rate is used as a probe. Both pump and probe are separated by 1° and incident normally on the sample. Here, X-ray absorption spectra is recorded in transmission geometry by an avalanche photodiode detector. A vector magnet (represented by a circular disk) is used to apply an alternating magnetic field to measure the change in XMCD as a function of pump-probe delay. Here, a solid black arrow represents the direction of the applied field. Since, the magnetic film has out-of-plane anisotropy, therefore, applied field and X-rays are parallel to the easy axis of magnetization.

The observed change in the demagnetization dynamics between the P and AP cases, is related to the difference in the relative spin orientations between SPHE and the Fe moment in $\text{Fe}_{74}\text{Gd}_{26}$. The red Gaussian curve in Fig.3 represents the SPHE pulse shape (G with FWHM = 420 fs), arriving at the $\text{Fe}_{74}\text{Gd}_{26}$ layer. The observed different dynamics between P and AP last significantly longer than the presence of the pump pulse itself. In order to evidence the dynamics of the difference between P and AP configurations, we plotted the difference using the fitted curves, as shown in Fig.3b. This figure shows that the difference between P and AP dynamics starts as soon as the SPHE pulse excites the film at $t = 0$. The differences between P and AP configurations as shown in Fig.3b evidences that the maximum SPHE induced effect occurs at a delay of $t = 0.5$ ps. It is not clear if this maximum corresponds to the SPHE pulse shape or if SPHE induced effects develop

specific ultrafast dynamics. By comparing with the pulse of the SPHE (G with FWHM = 420 fs), we highlight the fact that the spin-induced changes last up to $t = 2$ ps, much longer than the temporal superposition of the SPHE pump pulse. In Fig.3c, we show that at longer time scales, the difference in dynamics between P and AP orientations vanishes, which we assign to the limited mean free path and lifetime of the SPHEs. The dynamics of both orientations are therefore converged after ~ 3 picoseconds, and the magnetic recovery proceeds in a similar way for both P and AP configurations. Fig.3 additionally, shows that the difference reduces after 1 ps, vanishing after 3 ps. These essential features will be analyzed below, using theoretical, atomistic spin dynamics simulations.

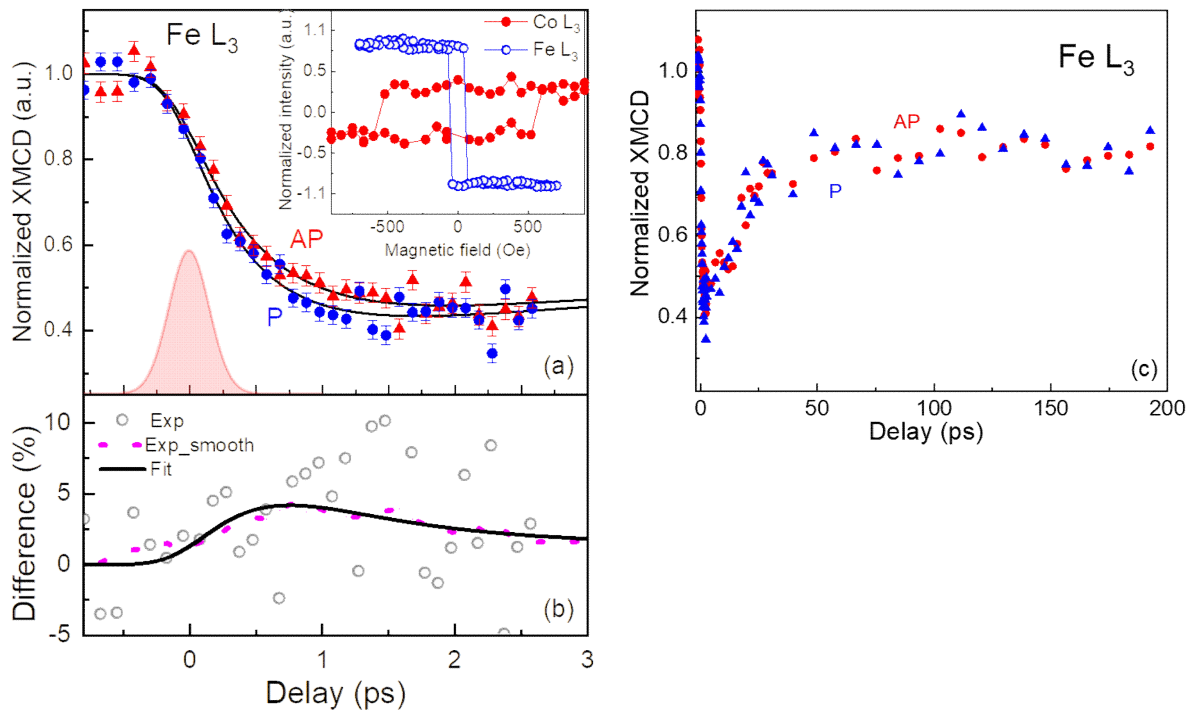


Figure 3: Spin polarized hot electron induced dynamics at Fe L_3 edge: Normalized time-resolved measurements of Fe L_3 XMCD at laser fluence of 120 mJ/cm^2 (absorbed fluence $F_{\text{abs}} = 3.2 \text{ mJ/cm}^2$) at $T = 80 \pm 20 \text{ K}$. To distinguish the SPHE effect, measurement is done in two configurations: Magnetization of Co is parallel (P) (blue curve) and Antiparallel (AP) (red curve) to Fe magnetization. Solid lines are the exponential fit with Gaussian convolution. The fitting of the P and AP experimental curves show characteristic demagnetization times of $470 \pm 80 \text{ fs}$, resp. $550 \pm 80 \text{ fs}$. (a) At a short time scale, i.e., below 2 ps, dynamics in the P case is faster and shows more demagnetization than AP case. The red Gaussian curve represents the SPHE pulse shape, arriving at the $\text{Fe}_{74}\text{Gd}_{26}$. The error bars obtained for the TR-XMCD at the Fe L_3 edge as shown in a are

given by the standard deviation of the experimental data with respect to the fitting functions. Inset: The hysteresis measured at the Co and Fe L₃ resonance edges. This indicates that the coercivity of Co/Pt layer ($H_C = 550$ Oe) is larger than the FeGd ($H_C = 100$ Oe) and ensures the maximum spin polarization from Co/Pt. (b) Normalized difference of the demagnetization dynamics between the P and AP cases obtained at the Fe L₃ edge (open symbols) superposed to the smoothed data (magenta dash line). The solid black line is the normalized difference between P and AP fitted dynamics, as given in Fig 3a. A maximum for the difference between both cases is found around 0.5 ps. (c) Dynamics at a longer time scale. SP effect vanishes after 2 ps due to limited mean free path and lifetime of those SPHEs.

Ultrafast demagnetization in Fe₇₄Gd₂₆. The case of Gd.

In Fig.4, we show the same experiment with the focus on the Gd 4f moment, recorded by measuring the dynamics at Gd M₅ edge, at a fluence of 40 mJ/cm². The ultrafast dynamics measured in P (blue) and AP (red) configurations are shown for short (Fig.4a) and long (Fig.4b) time ranges. Note that the values for Fe (Fig.3) and Gd (Fig.4) are normalized to 1. The lower fluence used during the pump-probe experiments at Gd M₅ edge explains the fact that the amplitude of demagnetization is only about -35% compared to -55% at the Fe L₃ edge. This different demagnetization amplitude is not related to other physical or chemical reasons (see S.I. - Fig. 4, comparison of Fe – Gd dynamics).

Within the achieved experimental noise level Fig.4 evidences no difference between P and AP configurations. We thus show only a double exponential fit with a characteristic demagnetization time of 900 ± 50 fs, typical times for FeGd alloys. Theoretical calculations (see below) also show that the expected differences between P and AP should be smaller for Gd M₅ than for Fe L₃, when using fluences that are appropriate to the experimental data of Fe and Gd. The larger X-ray cross section at the Gd M₅ edge compensates for the lower concentration in Gd M₅ compared to Fe L₃ and cannot explain the larger noise level at Gd M₅. However, this noise level can be attributed to the lower experimental laser fluence and, thus, to lower demagnetization amplitude compared to for Fe L₃. We note that the slicing facility's X-ray pulse stability varies between different experimental weeks, contributing to different noise levels for similar acquisition statistics.

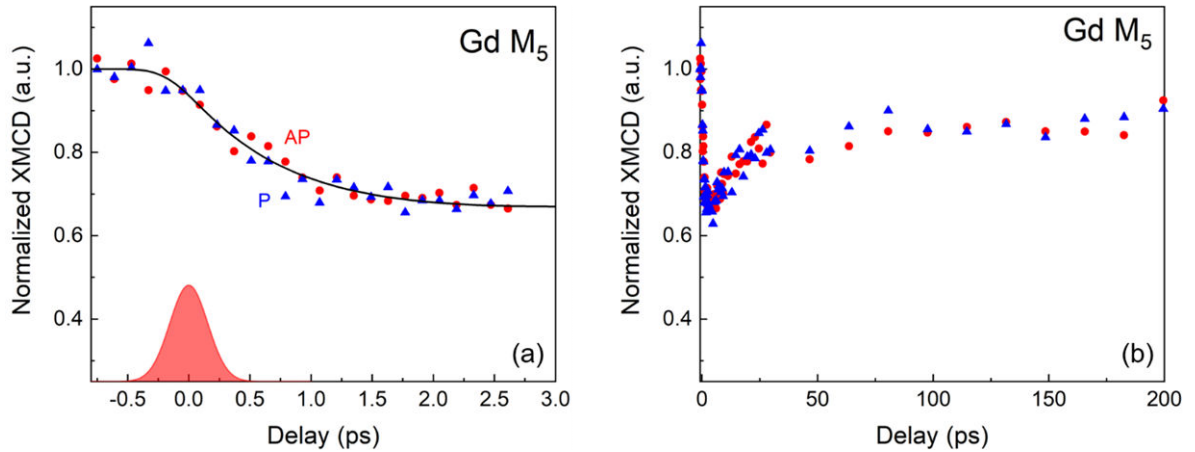


Figure 4. Spin polarized hot electron induced dynamics at the Gd M_5 edge, for short (a) and long (b) time scales. (a) Normalized experimental time-resolved measurements of Gd M_5 XMCD were obtained from the transmission signal at a laser fluence of 40 mJ/cm^2 (absorbed fluence $F_{\text{abs}} = 1.2 \text{ mJ/cm}^2$) and at $T = 140 \text{ K}$ working temperature. The measurements are done in two configurations: Magnetization of Co is parallel (P) (blue curve) and Antiparallel (AP) (red curve) to Fe magnetization. The solid black line represents the exponential fit with Gaussian convolution. We obtained the characteristic demagnetization time, $\tau_{\text{Gd}} = 900 \pm 100 \text{ fs}$. (b) Dynamics at a longer time scales showing similar dynamics for P and AP. Note that the statistics is not the same between 30 ps and 200 ps than at short time scales.

Simulated ultrafast demagnetization in $\text{Fe}_{74}\text{Gd}_{26}$.

To study the ultrafast demagnetization dynamics of $\text{Fe}_{74}\text{Gd}_{26}$, we performed atomistic spin-dynamics simulations⁴⁰ (see Methods section for simulations details). To analyze the experimental data, we have created a simulation cell consisting of 1600 atoms distributed inhomogeneously. In these simulations, we have followed theoretical and experimental studies suggesting that in amorphous compounds, the concentration of Fe and Gd varies in the sample⁴¹. In particular, we consider an amorphous alloy with an average concentration of $\text{Fe}_{74}\text{Gd}_{26}$ (as shown in Supplementary Information), however, some areas in the alloys are 6% richer in iron and some are 6% richer in gadolinium than the nominal concentration of $\text{Fe}_{74}\text{Gd}_{26}$. In our simulations, we assume that the hot electron pulse leads to an increased electron temperature in the $\text{Fe}_{74}\text{Gd}_{26}$ sample. The electronic temperature rise is accounted for by using a three-temperature model (3TM), that allows for heat to

flow between electron-, lattice- and spin reservoirs. The 3TM was proposed in the pioneering work of Beaurepaire et al.⁶ to calculate spin, lattice, and electron temperatures during ultrafast demagnetization dynamics. The model assumes three thermalized reservoirs, in particular, spin, lattice, and electron connected by electron-spin G_{es} , electron-lattice G_{el} , and spin-lattice G_{sl} coupling coefficients. When the electronic temperature increases (in the present case due to the hot electron pulse), the rise of spin- and lattice temperatures is mediated by these coupling coefficients G_{es} , G_{el} , G_{sl} . Parameters and details can be found in the Methods section and Supplementary Information. To analyze as closely as possible the experimental measurements presented above, we study separately iron and gadolinium magnetization dynamics in amorphous $\text{Fe}_{74}\text{Gd}_{26}$. The exchange interactions used in the simulations are reported in Ref.⁴¹. The other parameters for our simulations are chosen to accomplish a good comparison with the experimental data by carefully studying the impact of simulation parameters on the magnetization curve. In particular, the simulation parameters, such as the spin transfer torque, Gilbert damping α , electron-spin-, electron-phonon, and spin-lattice coupling in the three temperature models, will impact all the resulting aspects of the magnetization dynamics. The details of how these parameters influence the dynamics of $\text{Fe}_{74}\text{Gd}_{26}$ is shown in Supplementary Information.

After optimization of the simulated dynamics with our experimental results, we obtained, with one marked difference that we will return to below, a reasonable agreement between simulations and the experimental data recorded at the Fe L_3 edge during the first ~ 2 picoseconds of the magnetization dynamics (Fig.5). The sensitivity of the simulated data with respect to parameter choice is analyzed in detail, shown in Figs. S6-S11 in Supplementary Information. Most notable the simulations shown in Fig.5 reproduce the overall shape of the experimental curves, both when it comes to the position of the minimum of the M/M_0 curve (at 1.5 - 2 ps) as well as the overall shape of the M/M_0 demagnetization curve. In fact, simulations and experiment are basically on top of one another, with one marked exception, the simulated results with parallel STT fit perfectly the experimental results for AP configuration and simulated results with antiparallel STT fit perfectly the experimental results for P configuration, which is contrary to what is expected from the angular momentum transfers schematically shown in Fig.1. We will return to this enigma below.

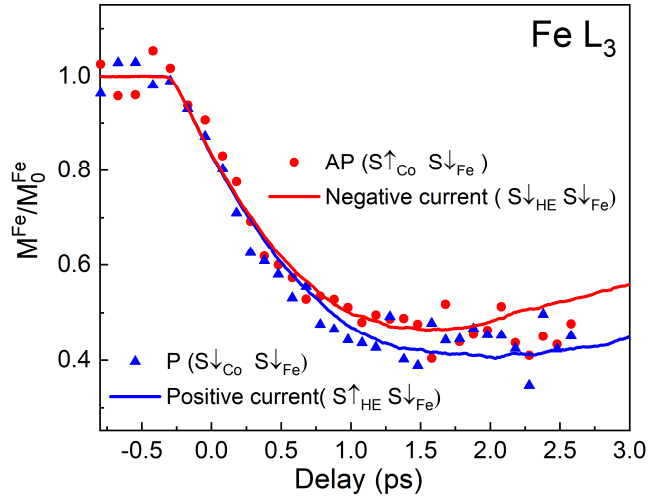


Figure 5. Magnetization dynamics of Fe in amorphous $\text{Fe}_{74}\text{Gd}_{26}$. Experimental and Simulated demagnetization dynamics by TR-XMCD and atomistic spin dynamics of Fe in $\text{Fe}_{74}\text{Gd}_{26}$ for 120 mJ/cm^2 incident and 3.2 mJ/cm^2 absorbed fluences. The laser fluence value has been adjusted to fit our experimental data. The blue (red) symbols are the experimental results for the P(AP) configurations. Solid lines in blue (red) are the simulations for the antiparallel (parallel) STT and the associated positive (negative) spin currents. In simulations the spin current polarization is defined as “positive” for the antiparallel orientation to the Fe 3d spins, so that the SPHE polarization is opposite to the Co moments, shown by the arrows in the figure legends.

Similarly, the simulated results for gadolinium are also in very good agreement with experimental measurement, as shown in Fig.6. In the simulations for Gd, we adjusted the heat-driven dynamics induced by the absorbed HE pulse by a factor of 0.4 in comparison to the data for Fe, which corresponds to the reduction of the IR incidence fluence between both experiments (The nominal fluence ratio is somewhat lower: 40 mJ / 120 mJ = 0.3). We assign the difference to the limited accuracy of laser fluence determination $\pm 20\%$, mostly because of uncertainties with the laser spot-size. Parameters in the simulations, such as Gilbert damping, and heat transfer parameters of the 3TM, influence the demagnetization amplitude of both sub-lattices. These can in the experimental samples differ for iron and gadolinium, while in the simulations presented here, we use for simplicity the same values for both sub-lattices. This may lead to a slight underestimation/overestimation of Fe and Gd demagnetization amplitudes. By deviating from the experimental estimate of the heat

provided by the hot electrons, we compensate for these differences. These results in simulated data which are in rather good agreement with observations (see Fig.6).

We now focus on the role of Gd in the amorphous $\text{Fe}_{74}\text{Gd}_{26}$ alloy. As shown in Figure 6, the demagnetization for gadolinium shows smaller amplitudes and a slower demagnetization dynamic than what is observed for Fe (Fig.5) while the experimental statistics does not allow drawing conclusions about the difference between P and AP cases. However, from the simulations, it can be evidenced that for gadolinium, the parallel and antiparallel STT simulations lead to slightly different demagnetization dynamics (Fig.6). Even with the small difference in the simulated curves, we are able to demonstrate that the acceleration of the demagnetization appears for a STT opposite compared to that for Fe, which is consistent with the ferrimagnetic state of the FeGd alloy investigated here.

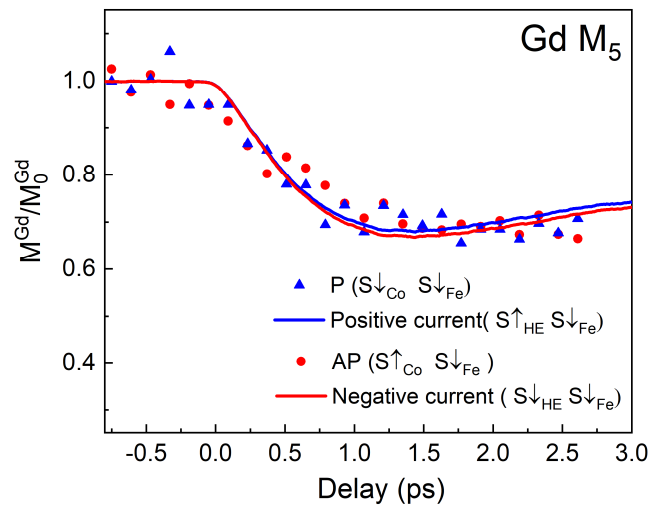


Figure 6. Magnetization dynamics of gadolinium in amorphous $\text{Fe}_{74}\text{Gd}_{26}$. Experimental and Simulated demagnetization dynamics by TR-XMCD and atomistic spin dynamics of Gd in $\text{Fe}_{74}\text{Gd}_{26}$ for 40 mJ/cm^2 incident and 1.2 mJ/cm^2 absorbed fluences. The last fluence has been adjusted to fit our experimental data. The blue (red) symbols and lines are the results for the P (AP) configurations. Solid lines in blue (red) are the simulations for the antiparallel (parallel) STT and the associated positive (negative) spin currents. In simulations the STT spin current polarization is defined as “positive” for the antiparallel orientation to the Fe 3d spins, shown by the arrows in the figure legends.

In order to investigate if the absence of splitting between curves labelled P and AP observed at the Gd M_5 edge is only due to the lower fluence used for Gd, the theoretical simulations were extended to absorbed fluences of 3.2 mJ/cm^2 , which is same as used in the simulations for Fe L_3 (Fig.5). Figure 7 shows the so-simulated dynamics for Gd 4f moments for parallel and antiparallel STT. The limited, but discernible, differences observed for Gd at these larger fluences indicate that significantly better experimental statistics would be needed at the Gd M_5 edge to evidence these small effects. In the experimental results reported here, taken at the slicing station at BESSY, this was not possible to achieve.

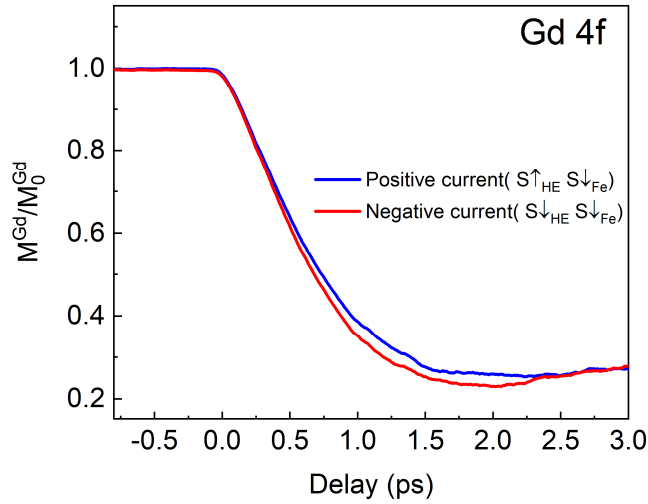


Figure 7: Calculated magnetization dynamics of Gd 4f in amorphous $\text{Fe}_{74}\text{Gd}_{26}$. Compared STT effect (difference between positive and negative STT) for both absorbed fluences at Gd in amorphous $\text{Fe}_{74}\text{Gd}_{26}$. The blue and red lines are simulations for opposite signs of spin polarized currents (Positive and negative) combining heat-driven demagnetization dynamics with STT. Gilbert damping value $\alpha = 0.1$, hot electron absorbed pulse fluence of 3.2 mJ/cm^2 .

Discussion

In this work, we have investigated experimentally the induced effect of ultrashort pulses of SPHE on the ultrafast demagnetization of amorphous $\text{Fe}_{74}\text{Gd}_{26}$ with an out-of-plane magnetic anisotropy. The

pump-probe measurements at Fe L_3 edge reveal not only faster demagnetization dynamics of the Fe 3d moments in the case of P configuration compared to AP configuration but also a reduction in the demagnetization amplitude for the AP configuration. A similar experiment performed at Gd M_5 edge did not show a sizable impact of spin polarized electrons, most probably due to weaker P/AP effects.

Accompanying experiments, we employed atomistic spin dynamics simulations, that utilized the Landau-Lifshitz Gilbert (LLG) equation. In these simulations it was assumed that the hot electron pulse leads to a rise of the electronic temperature of $Fe_{74}Gd_{26}$, followed by an increase in lattice- and spin temperature that we model with the 3-temperature model (considering the lattice temperature). In addition, the atomistic modeling considered a dynamic mechanism based on the spin transfer torque (STT), where spin angular momentum of an electric current couples with local magnetic moments of the material. Within this framework, it was found to be possible to reproduce the acceleration of the dynamics observed for the Fe sublattice and predict the effects for the Gd sublattice. The calculations show that, using a limited set of reasonable parameters (see Table 1 in Supplementary Information) belonging to the ferrimagnetic $Fe_{74}Gd_{26}$ alloy, the time scales and amplitudes of spin dependent demagnetization can, with one noticeable exception to be discussed shortly, be reproduced assuming a 100 % spin polarization of the SPHE pulses. The simulations show a very important result considering the spin polarization induced demagnetization dynamics in Fe and Gd sublattices. A spin polarization of the SPHE that provides a STT that is parallel to the Co moment (Fig.1) results in opposite dynamics to that observed in experiments, when it comes to the splitting between dynamics of the P and AP configurations (Fig.5). In contrast, a STT with a spin polarization coupled antiparallel to the Co moment reproduces almost perfectly the dynamics of the here investigated system, including the splitting between P and AP couplings. These results show similar trends as observed by Igarashi et al., in a spin valve structure.¹⁹ Based on our work and theoretical calculations, we conclude that the outgoing SPHE current from the Co/Pt stack has opposite spin polarization than the Co magnetization and that this explains the experimental results. The microscopic mechanism behind the opposite Co moment and the spin polarization of the electric current (used in STT) can be traced to the minority spin polarization of electron states close to the Fermi level of fcc Co⁴². The mechanism we hence propose is that SPHE generated by the 1.5eV laser pump, thermalizes during the propagation of top Pt(6)/ Cu(60) layers. We know

that only during the propagation through Pt the thermalization can happen whereas in Cu much less scattering of the HE should happen. The multiple scattering during the propagation through 6 nm Pt could thus lead to the thermalization ($E \sim 0.1$ eV) of the HE current towards the Co/Pt polarizer, where minority spin-polarization is generated.

Finally, considering simple macroscopic arguments of angular momentum conservations in the spin valve, we estimate that a maximum of angular momentum loss ($\sim 4.5 \mu_B$) in Co/Pt will be taken out from the multilayer (3nm thick Co film times $1.5 \mu_B/\text{at}$) which can be transferred to the FeGd alloy (at $t = t_0$, a 15nm thick FeGd film, times $2 \mu_B/\text{at} = 30 \mu_B$). We thus expect at maximum a change of 12% in the angular moment of the FeGd alloy due to the spin effect in HE induced demagnetization, assuming a complete quenching of the Co/Pt film and a 100 % transfer efficiency. It seems thus reasonable to measure at Fe L_3 edge a limited P/AP effect of 4 %.

Qualitative estimations of the relative effects in Fe and Gd in the FeGd alloy can be discussed from a simple energy point of view. In the simulations we propose a double contribution to the demagnetization, where the first is heat-driven by the HE energy transfer to the electronic system, whereas the second is provided by the energy transferred by the spin polarization of SPHE, and is modeled in our work by a STT. Double pulse induced dynamics has also been reported recently to explain switching mechanisms^{19,43,44}. Considering previous published results⁴⁵, we expect that in RE-TM alloys the RE and TM sublattices show opposite changes (acceleration or deceleration of the dynamic) when temperature is increased towards T_C ⁴⁵. In $\text{Fe}_{74}\text{Gd}_{26}$, we have $T_C = 500\text{K}$ which leads to: $T_C - T = 500 - 140 = 360$ K. The proximity to T_C could thus explain similar characteristic times for Fe and Gd sublattices as shown in S.I. figure 4 for HE induced dynamics. In FeGd assuming that in P configuration (blue symbols in figure 5), a supplement of energy flows into the 3d Fe, compared to AP, then we could expect from a temperature dependent model, that the excess energy raises the electron temperatures in the FeGd alloy leading to an acceleration of 3d Fe and to a deceleration of 4f Gd dynamic. This is what is observed here for FeGd. However, this is opposite to the previously studied CoDy system which demonstrates that the temperature dependent accelerations - decelerations are compositionally dependent on the RE-TM system⁴⁵.

Methods

Sample preparation and magnetic properties of the alloy films: 15nm thick alloys have been grown by magnetron sputtering on Si₃N₄ membranes. Co-deposition with convergent Co, Pt and Fe, Gd flux was used to get amorphous Fe₇₄Gd₂₆ alloy films and Co/Pt multilayers.

Static XMCD and magnetic hysteresis were performed at the Co L₃, Fe L₃, and Gd M₅ edges at the ALICE Station at the PM3 beam line of the BESSY II synchrotron radiation source of the Helmholtz-Zentrum Berlin⁴⁸. Time-resolved XMCD: Time resolved XMCD was performed at the femtoslicing beam line of the BESSY II synchrotron radiation source of the Helmholtz-Zentrum Berlin^{7,33}. The magnetization dynamics have been measured by monitoring the transmission signal of circularly polarized X-rays, tuned to specific core level absorption edges as a function of a pump-probe delay. The dynamic XMCD contrast is obtained by subtracting the gated signals obtained with and without pump beam. The energy was set to the different Fe L₃, and Gd M₅ edges using the Bragg Fresnel reflection zone plate monochromator. The experiments have been performed with a pump-probe setup where the short X-ray pulses are synchronized with a femtosecond pump laser working at 800 nm, 3 kHz repetition rate with pulses of 60 fs. The X-ray pulse duration of about 100 fs in the femtoslicing operation mode ensures a global time resolution of ~ 130 fs (see refs.^{7,33} for details). The pump fluences used during our experiments were adjusted to 120 mJ/cm² for the study of the dynamics at the Fe L₃ edge and to 40 mJ/cm² for the Gd M₅ edge to get the demagnetization magnitudes of about 50% at the Fe L₃ edge and 35% at the Gd M₅ edge without altering the sample properties (alloy concentration, atomic diffusion, large DC heating).

Fitting procedure:

The physical quantities M(t) were derived (figure 3 and 4), using the rate equation of the two-temperature model with two exponential functions (equation 1):

$$F(t) = G(t) [C_0 + C_1 H(t - t_0) [1 - \exp(-(t - t_0)/\tau_{th})] \exp(-(t - t_0)/\tau_s)] \quad (1)$$

where G(t) is the Gaussian function defining the total time resolution of the experiment (425 fs), τ_{th} and τ_{s-ph} are the thermalization time and the relaxation time from the spin system to other systems (lattice, external bath), t_0 is the delay at which the temporal overlap of the pump and the probe is

achieved and $H(t - t_0)$ is the Heaviside function ($H(t - t_0) = 0$ if $t < t_0$, and $H(t - t_0) = 1$ if $t > t_0$) describing the energy transfer from the laser.

Atomistic spin dynamics simulations

In atomistic spin dynamics simulations, spin dynamics is governed by Landau-Lifshitz-Gilbert equation:

$$\frac{dm_i}{dt} = -\frac{\gamma}{1+\alpha^2} m_i \times (B_i + B_i^{fl}) - \frac{\gamma}{(1+\alpha^2)} \frac{\alpha}{m_i} m_i \times (m_i \times (B_i + B_i^{fl})) \quad (2)$$

where m_i represents an atomic magnetic moment, m_i and γ are the saturation magnetization and the gyromagnetic ratio correspondingly. α is the Gilbert damping parameter. We obtain an effective exchange field $B_i = -\partial H_{SD}/\partial m_i$ is obtained from the spin Hamiltonian, H_{SD} . In our simulations, we use a stochastic field, B_i^{fl} , as white noise with properties $\langle B_{i,\mu}^{fl}(t) B_{j,\nu}^{fl}(t') \rangle = 2D_M \delta_{ij} \delta_{\mu\nu} \delta(t - t')$

In particular, in these calculations, we employ $D_M = \alpha k_B T / \gamma m$

where T and k_B are temperature and Boltzmann constant respectively (please see Ref.⁴⁰). The formalism above is implemented in the UppASD⁴⁶ code which was used for all simulations in this work.

The magnetic Hamiltonian is described by

$$H_{SD} = -\frac{1}{2} \sum_{ij} J_{ij} m_i \cdot m_j \quad (3)$$

where J_{ij} is the exchange tensor.

Spin-transfer torque (STT) was proposed by Slonczewski and Berger for a description of the impact of incoming itinerant electrons on localized magnetic moments in magnetic materials (see ref.⁴⁷ and references therein). STT is taken into account by adding the following field to the Landau-Lifshitz-Gilbert equation:

$$\mathbf{B}_{STT} = B_{STT}^{eff} (\mathbf{m} \times \mathbf{p}) \quad (4)$$

where the strength of STT term B_{STT}^{eff} depends on the current density j_e (Am⁻²), and \mathbf{p} is the spin polarization. We considered the largest term from Eq. 12 in⁴⁷ since the other terms are found to be negligible for some layered structures⁴⁷. The values of j_e used in the simulations can be found in Supplementary Information.

Data availability

Correspondence and requests for materials should be addressed to C. Boeglin Address: IPCMS, 23, rue du Lœss, F-67034 STRASBOURG Cedex 02, France e-mail: christine.boeglin@ipcms.unistra.fr

References

1. Stanciu, C. D. *et al.* All-Optical Magnetic Recording with Circularly Polarized Light. *Physical Review Letters* **99**, 047601 (2007).
2. Radu, I. *et al.* Transient ferromagnetic-like state mediating ultrafast reversal of antiferromagnetically coupled spins. *Nature* **472**, 205–208 (2011).
3. Ostler, T. A. *et al.* Ultrafast heating as a sufficient stimulus for magnetization reversal in a ferrimagnet. *Nature Communications* **3**, 666 (2012).
4. Kirilyuk, A., Kimel, A. V. & Rasing, T. Laser-induced magnetization dynamics and reversal in ferrimagnetic alloys. *Reports on Progress in Physics* **76**, 026501 (2013).
5. Avilés-Félix, L. *et al.* Single-shot all-optical switching of magnetization in Tb/Co multilayer-based electrodes. *Scientific Reports* **10**, 5211 (2020).
6. Beaurepaire, E., Merle, J.-C., Daunois, A. & Bigot, J.-Y. Ultrafast Spin Dynamics in Ferromagnetic Nickel. *Physical Review Letters* **76**, 4250–4253 (1996).
7. Boeglin, C. *et al.* Distinguishing the ultrafast dynamics of spin and orbital moments in solids. *Nature* **465**, 458–461 (2010).
8. Koopmans, B. *et al.* Explaining the paradoxical diversity of ultrafast laser-induced demagnetization. *Nature Mater* **9**, 259–265 (2010).

9. Krauß, M. *et al.* Ultrafast demagnetization of ferromagnetic transition metals: The role of the Coulomb interaction. *Phys. Rev. B* **80**, 180407 (2009).
10. Zangrando, M. *et al.* The photon analysis, delivery, and reduction system at the FERMI@Elettra free electron laser user facility. *Review of Scientific Instruments* **80**, 113110 (2009).
11. Bigot, J.-Y., Vomir, M. & Beaurepaire, E. Coherent ultrafast magnetism induced by femtosecond laser pulses. *Nature Physics* **5**, 515–520 (2009).
12. Battiato, M., Carva, K. & Oppeneer, P. M. Superdiffusive Spin Transport as a Mechanism of Ultrafast Demagnetization. *Phys. Rev. Lett.* **105**, 027203 (2010).
13. Battiato, M., Carva, K. & Oppeneer, P. M. Theory of laser-induced ultrafast superdiffusive spin transport in layered heterostructures. *Phys. Rev. B* **86**, 024404 (2012).
14. Pankratova, M. *et al.* Heat-conserving three-temperature model for ultrafast demagnetization in nickel. *Phys. Rev. B* **106**, 174407 (2022).
15. Eschenlohr, A. *et al.* Ultrafast spin transport as key to femtosecond demagnetization. *Nature Materials* **12**, 332 (2013).
16. Schellekens, A. J., Kuiper, K. C., de Wit, R. R. J. C. & Koopmans, B. Ultrafast spin-transfer torque driven by femtosecond pulsed-laser excitation. *Nature Communications* **5**, 4333 (2014).
17. Bergeard, N. *et al.* Hot-Electron-Induced Ultrafast Demagnetization in Co / Pt Multilayers. *Physical Review Letters* **117**, 147203 (2016).
18. Lalieu, M. L. M., Helgers, P. L. J. & Koopmans, B. Absorption and generation of femtosecond laser-pulse excited spin currents in noncollinear magnetic bilayers. *Phys. Rev. B* **96**, 014417 (2017).
19. Igarashi, J. *et al.* Optically induced ultrafast magnetization switching in ferromagnetic spin valves. *Nat. Mater.* **22**, 725–730 (2023).
20. Remy, Q. Ultrafast magnetization reversal in ferromagnetic spin-valves: an s-d model perspective. Preprint at <http://arxiv.org/abs/2303.05907> (2023).
21. Ferté, T. *et al.* Ultrafast hot-electron induced quenching of Tb 4 f magnetic order. *Physical Review B* **96**, 144427 (2017).
22. Ferté, T. *et al.* Ultrafast demagnetization in buried Co₈₀Dy₂₀ as fingerprint of hot-electron transport. *Journal of Magnetism and Magnetic Materials* **485**, 320–324 (2019).
23. Eschenlohr, A. *et al.* Spin currents during ultrafast demagnetization of ferromagnetic bilayers.

J. Phys.: Condens. Matter **29**, 384002 (2017).

24. Stamm, C. *et al.* X-ray detection of ultrashort spin current pulses in synthetic antiferromagnets. *Journal of Applied Physics* **127**, 223902 (2020).

25. Malinowski, G. *et al.* Control of speed and efficiency of ultrafast demagnetization by direct transfer of spin angular momentum. *Nature Physics* **4**, 855–858 (2008).

26. Iihama, S. *et al.* Single-Shot Multi-Level All-Optical Magnetization Switching Mediated by Spin Transport. *Advanced Materials* **30**, 1804004 (2018).

27. Schellekens, A. J. & Koopmans, B. Microscopic model for ultrafast magnetization dynamics of multisublattice magnets. *Phys. Rev. B* **87**, 020407 (2013).

28. Mentink, J. H. *et al.* Ultrafast Spin Dynamics in Multisublattice Magnets. *Physical Review Letters* **108**, 057202 (2012).

29. Bergeard, N. *et al.* Ultrafast angular momentum transfer in multisublattice ferrimagnets. *Nature Communications* **5**, 3466 (2014).

30. Cornelissen, T. D., Córdoba, R. & Koopmans, B. Microscopic model for all optical switching in ferromagnets. *Applied Physics Letters* **108**, 142405 (2016).

31. Wei, J. *et al.* All-optical Helicity-Independent Switching State Diagram in Gd - Fe - Co Alloys. *Phys. Rev. Applied* **15**, 054065 (2021).

32. Stamm, C. *et al.* Femtosecond modification of electron localization and transfer of angular momentum in nickel. *Nature Materials* **6**, 740–743 (2007).

33. Holldack, K. *et al.* FemtoSpeX: a versatile optical pump–soft X-ray probe facility with 100 fs X-ray pulses of variable polarization. *J Synchrotron Rad* **21**, 1090–1104 (2014).

34. Stohr, J. *Magnetism*. (Springer, Berlin, Heidelberg, 2006). doi:10.1007/978-3-540-30283-4.

35. Thole, B. T., Carra, P., Sette, F. & Van Der Laan, G. X-ray circular dichroism as a probe of orbital magnetization. *Phys. Rev. Lett.* **68**, 1943–1946 (1992).

36. Carra, P., Thole, B. T., Altarelli, M. & Wang, X. X-ray circular dichroism and local magnetic fields. *Phys. Rev. Lett.* **70**, 694–697 (1993).

37. Pankratova, M. *et al.* Heat-conserving three-temperature model for ultrafast demagnetization of 3d ferromagnets. Preprint at <http://arxiv.org/abs/2308.08996> (2023).

38. Lichtenberg, T., Beens, M., Jansen, M. H., Koopmans, B. & Duine, R. A. Probing optically induced spin currents using terahertz spin waves in noncollinear magnetic bilayers. *Phys. Rev. B* **105**, 144416 (2022).

39. Choi, G.-M., Min, B.-C., Lee, K.-J. & Cahill, D. G. Spin current generated by thermally driven ultrafast demagnetization. *Nature Communications* **5**, 4334 (2014).
40. Eriksson, O., Bergman, A., Bergqvist, L. & Hellsvik, J. *Atomistic Spin Dynamics: Foundations and Applications*. (Oxford university press, 2017).
41. Chimata, R. *et al.* All-thermal switching of amorphous Gd-Fe alloys: Analysis of structural properties and magnetization dynamics. *Phys. Rev. B* **92**, 094411 (2015).
42. Moruzzi, V. L., Janak, J. F. & Williams, A. R. II - CALCULATIONS. in *Calculated Electronic Properties of Metals* (eds. Moruzzi, V. L., Janak, J. F. & Williams, A. R.) 11–22 (Pergamon, 1978). doi:10.1016/B978-0-08-022705-4.50005-3.
43. Remy, Q. *et al.* Accelerating ultrafast magnetization reversal by non-local spin transfer. *Nat Commun* **14**, 445 (2023).
44. Liu, D., Jiang, C., Wang, N. & Xu, C. Minimum separation between two pump pulses for ultrafast double magnetization switching in GdFeCo. *Applied Physics Letters* **123**, 162401 (2023).
45. Ferté, T. *et al.* Laser induced ultrafast 3d and 4f spin dynamics in CoDy ferrimagnetic alloys as a function of temperature. *Journal of Magnetism and Magnetic Materials* **530**, 167883 (2021).
46. Uppsala atomistic spin dynamics <https://github.com/UppASD/UppASD>.
47. Meo, A., Cronshaw, C. E., Jenkins, S., Lees, A. & Evans, R. F. L. Spin-transfer and spin-orbit torques in the Landau–Lifshitz–Gilbert equation. *J. Phys.: Condens. Matter* **35**, 025801 (2023).
48. R. Abrudan, F. Brüßing, R. Salikhov, J. Meermann, I. Radu, H. Ryll, F. Radu, and H. Zabel, Alice—an advanced reflectometer for static and dynamic experiments in magnetism at synchrotron radiation facilities, *Review of Scientific Instruments* **86** (2015).

Acknowledgments

We are indebted to R. Mitzner and M. Mawass for help and support during the femtoslicing experiments. This work was supported by funding from the European Union's Horizon 2020 research and innovation programme under the Marie Skłodowska-Curie grant agreement number 847471, by the "Agence Nationale de la Recherche" in France via the project ANR MEDYNA, and by the German Ministry of Education and Research BMBF Grant 05K10PG2 (FEMTOSPEX). This work was financially supported by Olle Engkvist Foundation. Support from STandUP and eSSSENCE is also acknowledged. O.E. also acknowledge support from the Swedish Research

Council, the European Research Council (ERC) as well as the Wallenberg Initiative Materials Science for Sustainability (WISE) funded by the Knut and Alice Wallenberg Foundation (KAW), the Swedish Research Council and the Knut and Alice Wallenberg Foundation (KAW). Computations were enabled by resources provided by the Swedish National Infrastructure for Computing (SNIC/NAISS) at NSC, partially funded by the Swedish Research Council through grant agreement no. 2018-05973. R.A. acknowledge financial support by the German Federal Ministry of Education and Research BMFG project number 05K19WO61.

Author contributions statement

D.G., M.R., N.P., C.S-L., N.B. and C.B. performed the time resolved measurements and data exploitations. M.H. grew and characterized the samples. D.G., N.B., R.A. and C.B. performed the static temperature XMCD characterization. D.G. and C.B. wrote the first draft of the paper. A.B., O.E., and M.Pe initially designed the theoretical model. M.Pa. performed the simulations and calculations, M.Pa, A.B., B.S., S.E., O.E., and M.Pe analyzed the results and their interpretations. All authors discussed and contributed to the manuscript.

Additional Information

The authors declare no competing interests.

SUPPLEMENTARY INFORMATION:

Tuning of the ultrafast demagnetization by ultrashort spin polarized currents in multi-sublattice ferrimagnets.

Deeksha Gupta¹, Maryna Pankratova², Matthias Riepp¹, Manuel Pereiro², Biplab Sanyal², Soheil Ershadrad², Michel Hehn³, Niko Pontius⁴, Christian Schüßler-Langeheine⁴, Radu Abrudan⁴, Nicolas Berggaard¹, Anders Bergman², Olle Eriksson^{2,5}, and Christine Boeglin^{1*}

¹Institut de Physique et de Chimie des Matériaux de Strasbourg, UMR7504, CNRS et Université de Strasbourg, 67034 Strasbourg, France

²Department of Physics and Astronomy, Uppsala University, Box 516, SE-75120 Uppsala, Sweden

³Institut Jean Lamour, Université Henri Poincaré, Nancy, France

⁴Helmholtz-Zentrum Berlin für Materialien und Energie GmbH, Albert-Einstein Str. 15, 12489 Berlin, Germany

⁵Wallenberg Initiative Materials Science for Sustainability (WISE), Uppsala University, Box 516, SE-75120 Uppsala, Sweden

* christine.boeglin@ipcms.unistra.fr

I. EXPERIMENTAL DETAILS

A. Calculation of absorption profile

We used the transfer matrix method [1] to calculate the absorption profile of the IR pulse in the sample structure (shown in Figure 1).

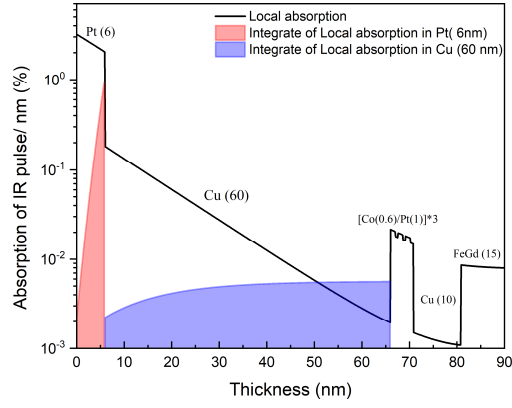


Figure 1. Absorption of IR intensity through the spin-valve structure. It shows that less than 10^{-3} is transmitted to the FeGd layer.

Elements	Refractive Index (800 nm)
Pt	$2.83 + 4.95 i^3$
Cu	$0.26 + 5.26 i^3$
Co	$2.53 + 4.88 i^2$
Fe	$2.94 + 3.39 i^2$
Ta	$1.09 + 3.73 i^3$

Table I Refractive indices at 800 nm wavelength used to calculate the absorption profile.

B. Variation of XMCD and coercive field with temperature

To set the experimental parameters, we performed static XMCD measurements using the ALICE reflectometer situated at the PM3 beamline at the BESSY II synchrotron source⁴. XAS spectra were recorded by employing two opposite magnetic fields ($\pm H$) in transmission geometry at Fe L₃, Co L₃ and Gd M₅ edges (fig 2 a). Additionally, we recorded the hysteresis of each element at their corresponding resonance edges as a function of temperature (fig 2 b). It is shown from the coercive field values in figure 2 that compensation temperature is above 300 K.

C. Estimation of sample temperature during pump-probe experiment

Time-resolved XMCD measurements were performed at the cryostat temperature of 80 K. Due to limited photon flux during slicing mode, it's not possible to measure the hysteresis as a function of pump-probe delay. Therefore, in order to examine the sample temperature during the pump-probe experiment, we measured the time-resolved hysteresis using X-ray pulses of duration ~ 50 ps in the normal synchrotron mode, before switching to the femto-slicing mode. Figure 3 shows the hysteresis measured with Laser off and Laser on at $t = 50$ picoseconds (ps). By comparing the coercive field values from the static measurement data (fig 2), the temperature at the delay, $t = 50$ ps, is calibrated to be 220 K (represented by the cyan color dot in Fig 2).

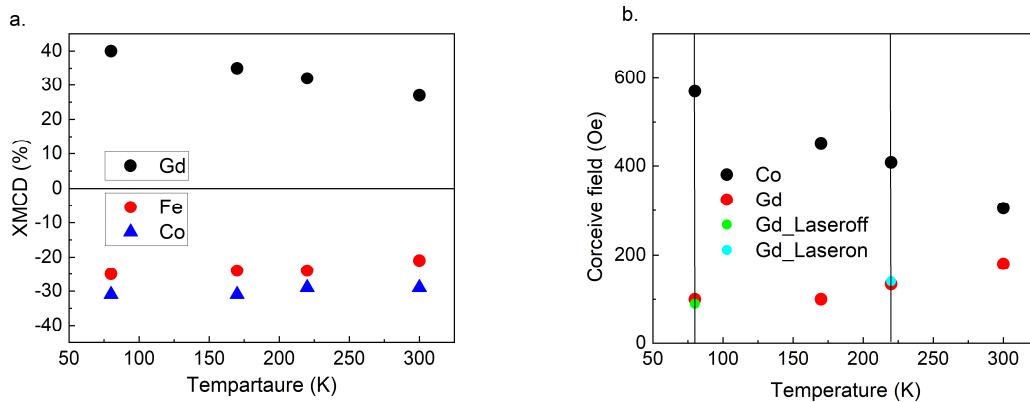


Figure 2. (a) Shows static XMCD (black (Gd M5), red (Fe L3), and blue (Co L3) points) as a function of temperature (b) shows coercive fields (black and red points) as a function of temperature for the spin-valve structure at the Co L3 and Gd M5 edges. As supplement information, we show (green and cyan points) the coercive fields measured at the GdM5 edge, comparing the coercive fields without laser and with the laser (at a delay of $t = 50$ ps). We observe that the coercive field at Gd M5 using the laser matches the static coercive field at $T = 220$ K. This data defines the sample temperature during pump-probe experiments at a delay of 50 ps after the IR and HE excitation. Note that $T = 80$ K is the cryostat temperature without any additional DC heating, which may occur during the pump-probe experiment.

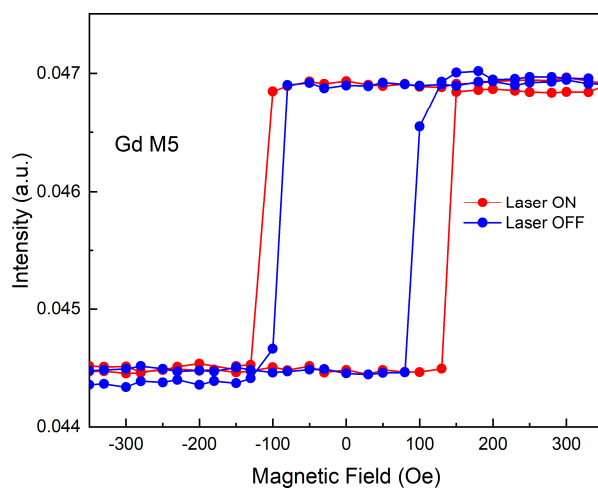


Figure 3. Hysteresis recorded at the Gd M₅ edge with and without the laser at a delay of $t = +50$ ps at an incident IR fluence of 40 mJ/cm^2 .

D. Magnetization dynamics of Fe₇₄Gd₂₆

Figure 4 shows the magnetization dynamics measured at IR laser fluence of 40 mJ/cm^2 . These measurements were performed during the same beamtime and with the same experimental conditions.

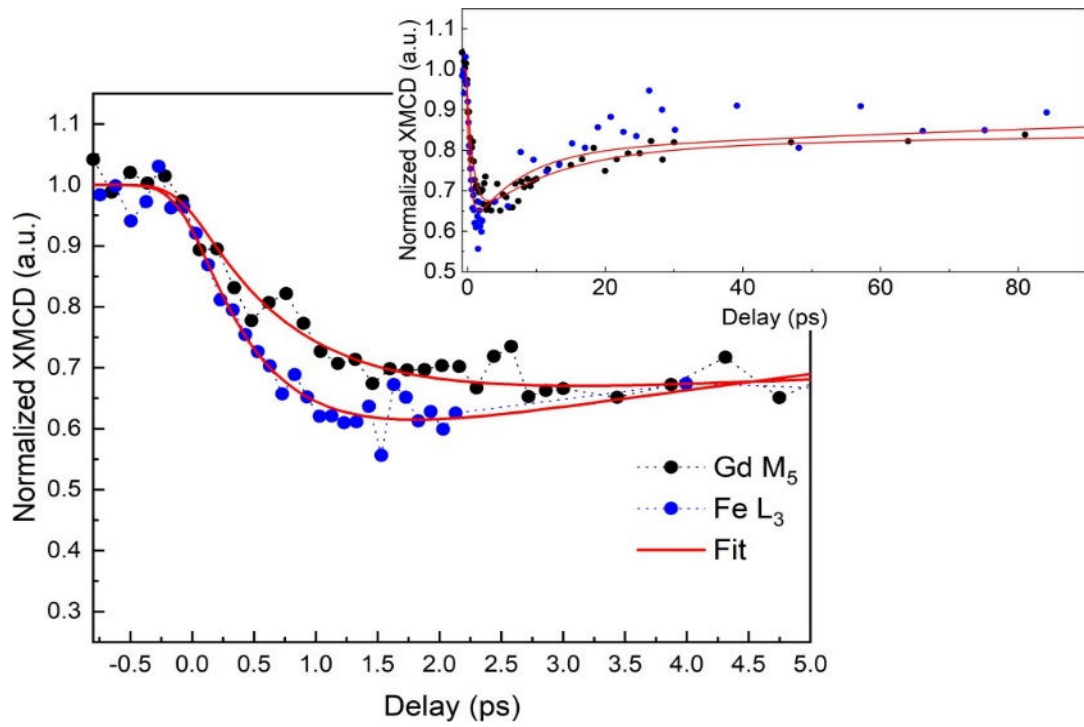


Figure 4. Dynamics induced by unpolarized hot electrons measured at Fe L₃ and Gd M₅ edges at incident IR laser fluence of 40mJ/cm² and simulated with absorbed fluence of 1.2 mJ/cm².

E- IMPACT OF SIMULATION PARAMETERS ON MAGNETIZATION DYNAMICS

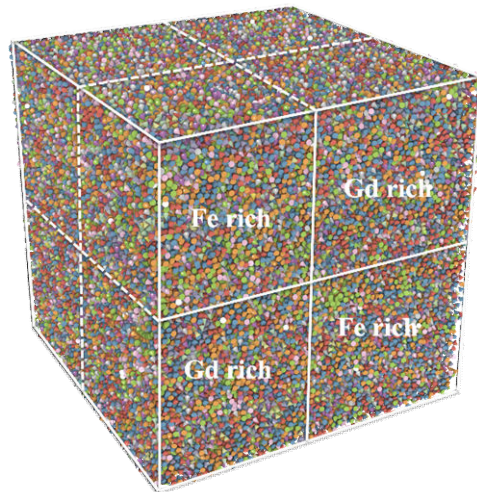


Figure 5. Schematic figure showing the heterogeneous amorphous samples of $\text{Fe}_{74}\text{Gd}_{26}$ with marked areas of areas richer in Gd or in Fe.

In our atomistic spin dynamics calculations, we use amorphous $\text{Fe}_{74}\text{Gd}_{26}$ with 1600 atoms in the simulation cell with periodic boundary conditions. Our simulation sample with areas rich in Gd or Fe is shown in Fig.5. The simulation parameters, such as hot electrons pulse, current density, Gilbert damping α , and electron-spin G_{es} , electron-phonon G_{el} , spin-lattice G_{sl} coupling in three temperature models will impact the resulting magnetization dynamics, its amplitude, demagnetization, and remagnetization rates. Here, we demonstrate the influence of these parameters Figs.6-11. In particular, we start by varying hot electrons pulse used in our simulations on magnetization dynamics of iron and gadolinium in amorphous $\text{Fe}_{74}\text{Gd}_{26}$. In the Fig.6, we present the impact of fluence for both negative and positive current directions. The shaded areas correspond to the values interval 2.8

– 3.6 mJ/cm² for iron and 1.0 – 1.4 mJ/cm² for gadolinium. Then, we add a similar analysis for electron-spin coupling G_{es} , as one can see in Fig.7, electron-phonon G_{el} (Fig.8). In our simulations, presented in the main text, we do not consider spin-lattice coupling, as one can see in Fig.9 it is indeed not significant, especially for Gd, and leading mostly to slight change of the demagnetization amplitude. In addition, our simulations, presented in the main manuscript assume that the observed difference between parallel and antiparallel cases in the experiment is due to STT impact. Fig.10 shows our results are impacted by a change of STT values. One can observe, that, the difference between parallel and antiparallel cases is maintained, while STT is changed slightly. Finally, we demonstrate the impact of Gilbert damping in Fig.11. In all simulations, we keep all parameters fixed and vary only one of them, e.g. laser fluence in Fig.6. The solid lines on all graphs corresponding to simulations presented by solid lines in Figs.5-6 of main manuscript.

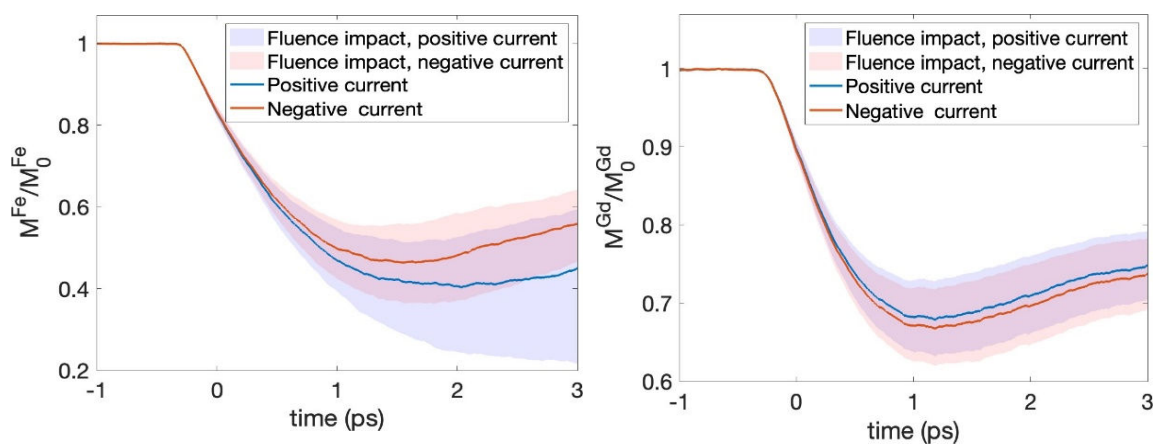


Figure 6. The impact of hot electrons pulse on magnetization dynamics of Fe (a) and Gd (b) in amorphous Fe₇₄Gd₂₆. Shaded areas demonstrate the fluence interval 2.8 – 3.6 mJ/cm² for iron and 1.0 – 1.4 mJ/cm² for gadolinium. The blue/red shaded areas/lines correspond to the cases of either positive or negative current in STT.

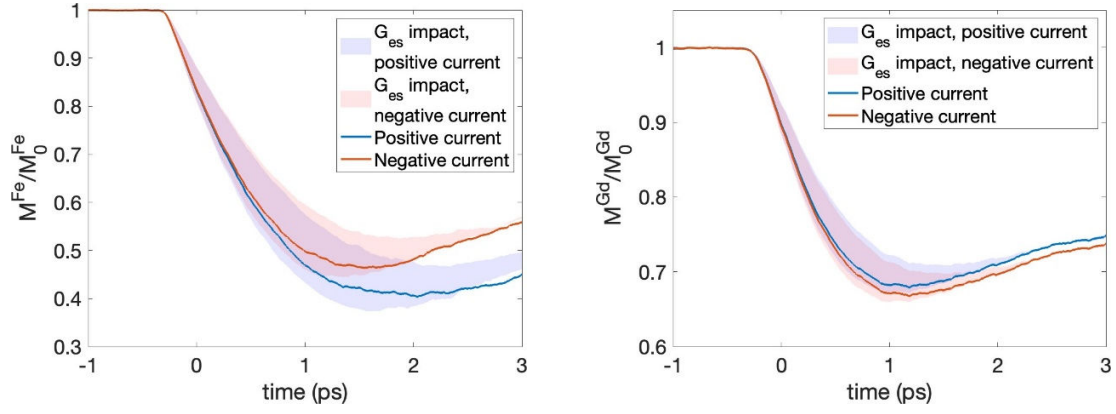


Figure 7. The impact of electron-spin coupling G_{es} on magnetization dynamics of Fe (a) and Gd (b) in amorphous Fe₇₄Gd₂₆. Shaded areas demonstrate the G_{es} interval $0.8 \times 10^{18} - 1.4 \times 10^{18}$ W/m³/K. The blue/red shaded areas/lines correspond to the cases of either positive or negative current in STT.

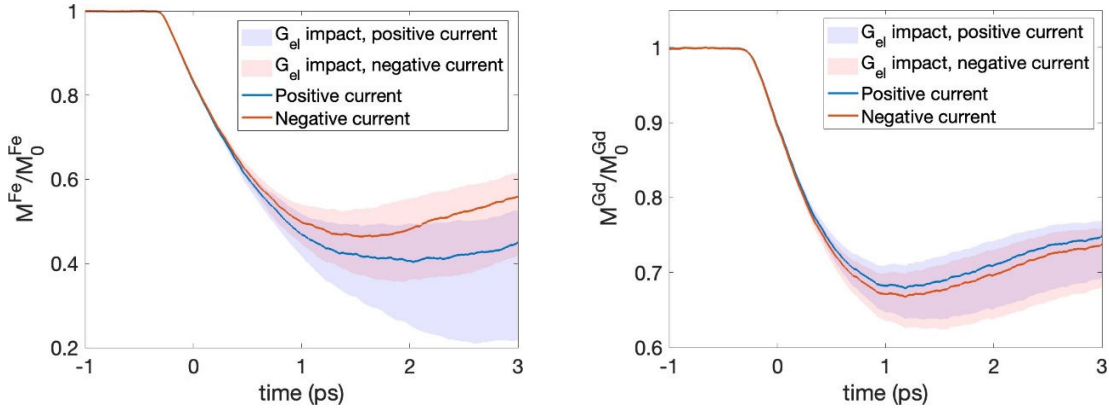


Figure 8. The impact of electron-phonon coupling G_{el} on magnetization dynamics of Fe (a) and Gd (b) in amorphous Fe₇₄Gd₂₆. Shaded areas demonstrate the G_{el} interval $4 \times 10^{17} - 1.2 \times 10^{18}$ W/m³/K. The blue/red shaded areas/lines correspond to the cases of either positive or negative current in STT.

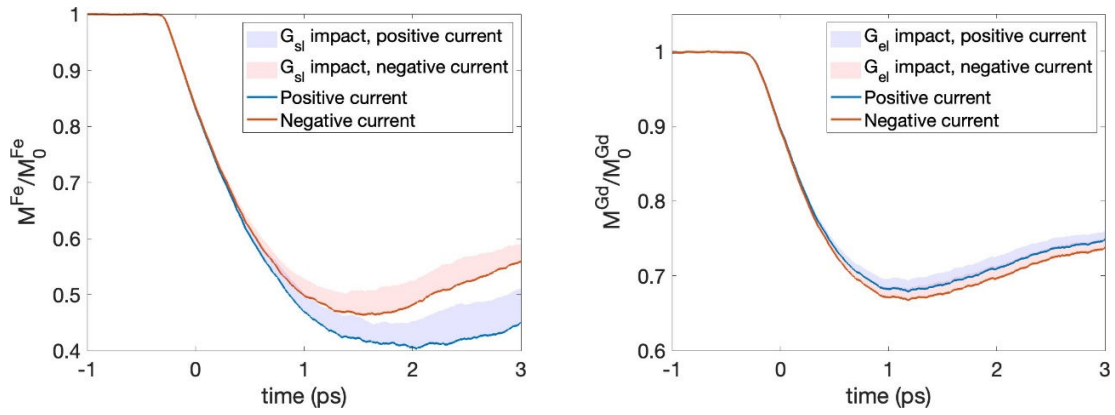


Figure 9. The impact of spin-lattice coupling G_{sl} on magnetization dynamics of Fe (a) and Gd (b) in amorphous $\text{Fe}_{74}\text{Gd}_{26}$. Shaded areas demonstrate the G_{el} interval $0.0 - 1 \times 10^{17} \text{ W/m}^3/\text{K}$. The blue/red shaded areas/lines correspond to the cases of either positive or negative current in STT.

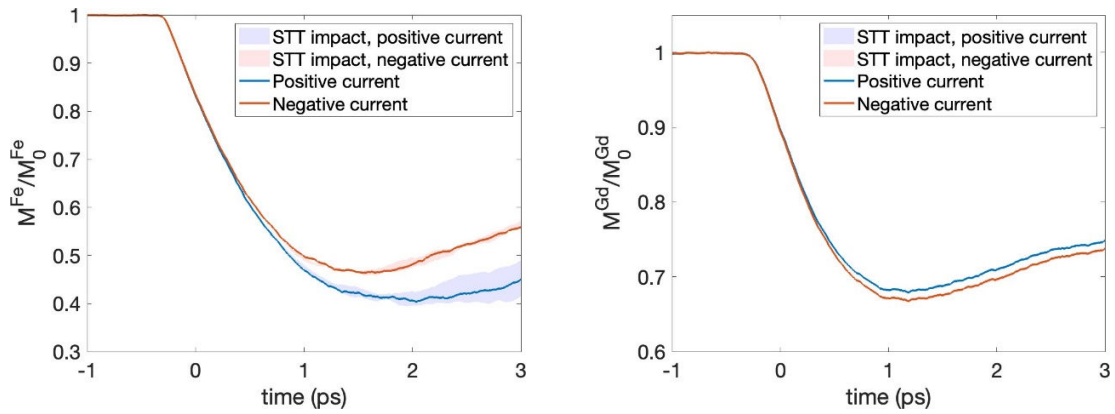


Figure 10. The impact of STT on magnetization dynamics of Fe (a) and Gd (b) in amorphous $\text{Fe}_{74}\text{Gd}_{26}$. Shaded areas demonstrate the STT interval. The blue/red shaded areas/lines correspond to the cases of either positive or negative current in STT.

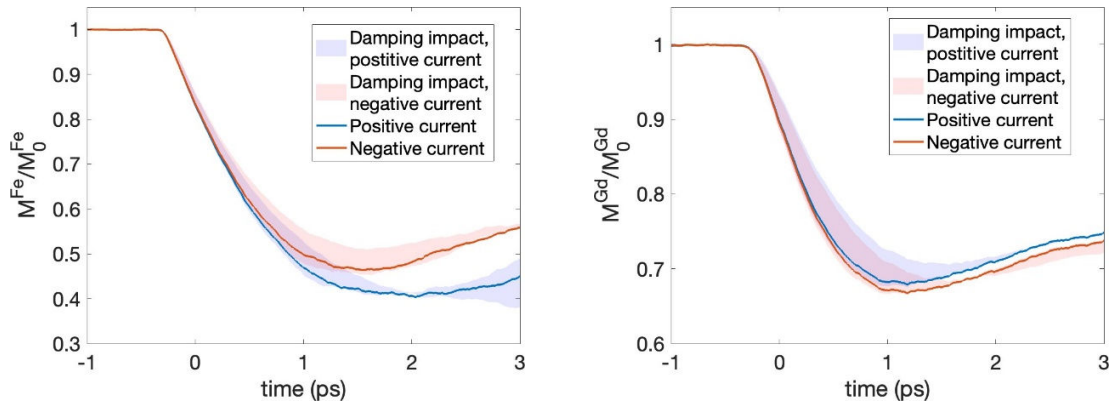


Figure 11. The impact of Gilbert damping α on magnetization dynamics of Fe (a) and Gd (b) in amorphous Fe₇₄Gd₂₆. Shaded areas demonstrate the α interval 0.05 – 0.12. The blue/red shaded areas/lines correspond to the cases of either positive or negative current in STT.

PARAMETERS USED IN THE SIMULATIONS

Parameter	Value
Gilbert damping α	0.1
Electron-spin coupling G_{es}	1.2×10^{18} W/m ³ /K.
Electron-phonon coupling G_{el}	8×10^{17} W/m ³ /K.
Spin-lattice coupling G_{sl}	0.0 W/m ³ /K.
Temperature	80 K
Current density (Fig. 5 and 7)	2.18×10^{10} A/m ²
Current density (Fig.6)	8.16×10^9 A/m ²

Table II. List of the parameters used in the simulations.

**F- Simulated element resolved demagnetization dynamics at high and low fluences
(Fe3d versus Gd4f).**

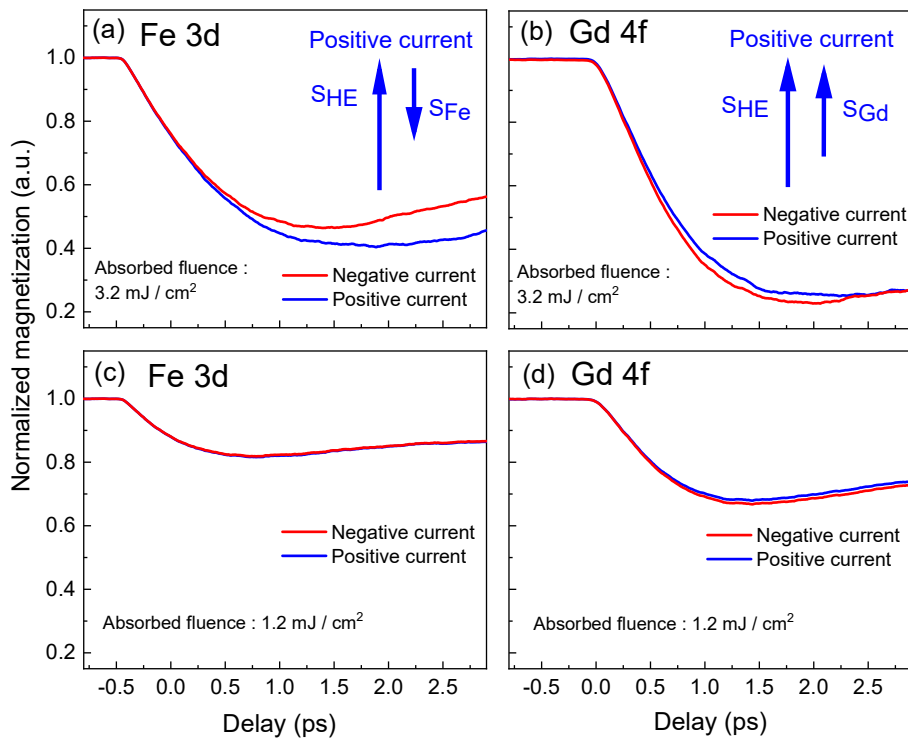


Figure 12. Simulated atomistic spin dynamics of Fe (a,c) and Gd (b,d) moments in $Fe_{74}Gd_{26}$ for the two absorbed fluence values (a,b) 3.2 mJ/cm^2 and (c,d) 1.2 mJ/cm^2 . The AP configuration in the SPHE currents leads to deceleration of the 3dFe and acceleration of the 4fGd dynamics.

References:

- 1- S. J. Byrnes, Multilayer optical calculations, arXiv preprint arXiv:1603.02720 (2016).
- 2- Johnson, P. & Christy, R. Optical constants of transition metals: Ti, V, Cr, Mn, Fe, Co, Ni, and Pd. *Physical Review B* **9**, 5056–5070 (1974).
- 3- Haynes, W. M., editor *Handbook of Chemistry and Physics*, CRC Press, 96 edition (2015-2016)
- 4- R. Abrudan, F. Brüssing, R. Salikhov, J. Meermann, I. Radu, H. Ryll, F. Radu, and H. Zabel, Alice— an advanced reflectometer for static and dynamic experiments in magnetism at synchrotron radiation facilities, *Review of Scientific Instruments* **86** (2015).